

An Optimization-Based Design Strategy for Centrifugal Compressors of Automotive Turbochargers and the Comparison of Five Particular Optimization Methods

Mert Alpaya¹

Department of Mechanical Engineering, Istanbul Technical University
34437 Istanbul, Turkey
alpaya@itu.edu.tr

Levent Kavurmacioglu

Associate Professor
Department of Mechanical Engineering, Istanbul Technical University
34437 Istanbul, Turkey
kavurmacio@itu.edu.tr

Cengiz Camci

Prof. of Aerospace Engineering, ASME Fellow (1392398)
Department of Aerospace Engineering, The Pennsylvania State University
16802 University Park, PA, USA
cxc11@psu.edu

ABSTRACT

It is possible to optimize a turbocharger's performance for a broad range of engine operating points. However, most of the turbochargers have distinctive performance characteristics independent of engine operation. Therefore, the correct way to obtain the maximum performance from an engine is to design its turbocharger for the specific engine performance map in mind. This paper deals with the effective use of computational methods to create optimal turbocharger compressors for realistic engine operating

¹ Corresponding author.

31 *conditions. The present process has four steps: preliminary analysis, throughflow analysis,*
32 *optimization, and Computational Fluid Dynamics (CFD) analysis. In the preliminary*
33 *analysis, gas dynamics and Euler turbomachinery equations are used to calculate the basic*
34 *dimensions. In the throughflow analysis, calculated dimensions are used to create a*
35 *parametric 3D geometry. A throughflow analysis generates the 2D flow results using the*
36 *meridional geometry of this 3D geometry. The main contribution of this research is the*
37 *five different optimization methods that are employed and compared. The efficiency of*
38 *the rotor is defined as the objective function to be maximized. A comparison of the five*
39 *optimization schemes showed that the genetic algorithm (GA) is the most suitable method*
40 *for the current design optimization problem. In the final step, a CFD solver is used to assess*
41 *the created design's final performance. The CFD results' validity are checked against a*
42 *reference compressor's test results. The present study also indicates that preliminary*
43 *sizing followed by a well-built throughflow analysis eliminates the need for a fully*
44 *parametric 3D CFD-based design.*

45 **1. Introduction**

46 Internal combustion engines' power production level is proportional to the amount of
47 air and fuel that passes through the cylinders. If one wants to downsize a machine for the
48 same power or make an engine have more power at the same size, the objective should
49 be to draw more air into the cylinders [1]. This task can be performed effectively by a
50 turbocharger. A turbocharger is a turbine-driven compressor that increases an internal
51 combustion engine's efficiency and power output by sending more compressed air into

52 the combustion chamber [2-5]. In passenger car applications, an internal combustion
53 engine's maximum efficiency is about 35%, while a turbocharged engine has nearly 40%
54 efficiency [6]. The early turbocharged engines were large diesel engines of marine, power
55 generation, and locomotive applications, but turbocharging made a slow penetration into
56 the automotive industry. Emissions regulations made the industry turn to turbocharge,
57 and most of the diesel engines and gasoline engines are now turbocharged [7-9]. The
58 optimum turbocharging solution can differ between gasoline and diesel engines as these
59 engines have distinctive characteristics [7, 10].

60 The vehicle can be optimized as a complete system of which the turbocharger is only
61 one component that interacts with many other parts of the system [7, 11]. The correct
62 selection of a turbocharger to build a complete engine-turbocharger system is challenging
63 because of many design considerations. Depending on the turbocharging application's
64 nature, the performance should be investigated in a wide range of operating points [12].

65 Automotive turbochargers consist of a centrifugal compressor, a central housing
66 rotating assembly, and a radial turbine. The compressor stage defines the performance
67 of a turbocharger. A centrifugal compressor stage comprises rotating and stationary
68 components. The air enters the impeller in the axial direction. In some cases, inlet guide
69 vanes are used to preswirl the air before entering the impeller. The flow is diffused
70 through the impeller and turned towards the radial direction at the impeller's exit so that
71 it leaves with a combination of radial and tangential velocities. At this point, the flow still
72 has substantial kinetic energy, and the diffuser recovers most of it. Finally, the air must

73 be collected and directed towards the inlet manifold, using a simple plenum or a volute
74 for additional diffusion [7, 13].

75 Since a turbocharger is a crucial component in terms of an engine's performance and
76 life, its design and matching characteristics with the engine need to be handled carefully.

77 Qiu et al. [14] described a method to design and optimize a turbocharger at a system level
78 using basic engine parameters and simple models for other commonly used components,
79 such as exhaust gas recirculation, wastegate, and intercooler. De Bellis et al. [15]
80 developed a 1D model to predict the device's performance maps based on its main
81 geometrical characteristics. The proposed model solves 1D flow equations inside the
82 rotating and stationary regions through the compressor and utilizes an advanced
83 geometrical module that can reproduce the impeller geometry based on a few linear and
84 angular geometrical data, easily measurable on the real part. Canova et al. [16] presented
85 a scalable modeling approach for characterizing flow and efficiency maps for automotive
86 turbochargers. Their model predicts the flow and efficiency maps of centrifugal
87 compressors and radial turbines of turbochargers as functions of their fundamental
88 design parameters. The proposed approach was validated using a database of
89 compressors and turbines. Nasser and Playfoot [17] developed a turbocharger selection
90 model based on 1D mass, momentum and, energy conversation equations for both
91 compressor and turbine. The proposed model contains heat transfer and loss calculation
92 sub-models for radial turbines and centrifugal compressors. The model was verified with
93 the test data of the turbocharger mounted on a diesel engine. Pakle and Jiang [18]
94 presented an approach to design centrifugal compressors for high-speed turbomachinery.

95 Their method consists of preliminary design, Finite Element Analysis (FEA), and
96 Computational Fluid Dynamics (CFD) steps, respectively. Parameterized hub and shroud
97 curves are modified based on the compressor's work coefficient in the preliminary design
98 phase. Favaretto et al. [19] developed a meanline model for the preliminary design of
99 automotive turbocharger compressors. The study introduced a 2D CFD-based
100 aerodynamic loss model modified according to fundamental flow quantities obtained
101 from 3D CFD analyses. Dombrovsky [20] conducted both model development and
102 experimental studies to present heat transfer and gas flow processes in turbochargers.
103 Dombrovsky created two different models to represent heat transfer and gas flow
104 phenomena. Dehner et al. [21] studied the compressor's behavior with a 1D engine
105 simulation code. The compressor performance in the model is represented through an
106 extrapolated steady-state map. Driving torque is applied to the turbocharger shaft instead
107 of using a separate turbine model. Im [22] developed a centrifugal compressor design and
108 analysis code that uses both one and two-dimensional thermo-fluid equations. The
109 developed tool calculates main flow properties such as pressure, temperature, velocity,
110 etc., at several points through the compressor for a specified set of geometry,
111 atmospheric conditions, rotational speed, and mass flow rate. The tool can be integrated
112 into commercial CFD and FEA packages. Schiff [23] presented a computer program that
113 allows inexperienced users to create 3D radial compressor geometries. The proposed tool
114 consists of different modes for preliminary impeller design, detailed impeller design,
115 impeller flow analysis, vaneless diffuser design, and vaned diffuser design. Buchman et al.
116 [24] presented a method for turbocharging single-cylinder engines. The proposed method

117 adds an air capacitor between the compressor outlet and the engine intake to cushion
118 the compressor output and provide pressurized air during the intake stroke. The zero
119 inertia and the infinite inertia models were used to model the turbocharger in the system.
120 The results of the theoretical study were validated against an experimental setup.
121 Tsukiyama et al. [25] presented a novel turbocharger that improves turbocharger's
122 response and fuel economy. The impellers of the compressor and turbine are adopted to
123 prevent flow separation by increasing the axial length and decreasing the radial length.
124 This approach helps to improve the surge limit and the compressor boost. Their design
125 also allows reducing the size of the turbine as the turbine flow capacity decreases.
126 Golovan et al. [26] presented a model that shows the relation between the power of a
127 two-stroke marine diesel engine and the turbocharger parameters like turbocharger
128 speed and scavenging air temperature. The results of their experimental studies were also
129 used to verify the simulation results. Their method proposed an alternative way to
130 estimate the power output of the engine.

131 The current investigation presents a unique design optimization method for centrifugal
132 compressors used in automotive turbochargers. The proposed method comprises
133 preliminary, throughflow, and CFD analyses. This manuscript also discusses the recent
134 efforts in carrying out numerical investigations, optimization methods, and experimental
135 studies of turbochargers. The results from five different optimization schemes are
136 presented and compared. The five optimization schemes employed include a response
137 surface based optimization (RSO), a non-linear programming based on quasi-Newton
138 approach (NLPQN), a non-linear programming method using the derivative-free method

139 (NLPDF), a pattern search based optimization (PS), and a genetic algorithm (GA). A
140 performance comparison of the optimization results from the five schemes is provided.
141 The current study shows that the choice of the optimization method is of critical
142 importance for improved turbocharger compressor designs. A performance-based
143 comparison of the optimization results from the five optimization schemes showed that
144 the GA is the most suitable method for the current design optimization problem. The
145 current method will allow designers to acquire maximum performance from an internal
146 combustion engine as the turbocharger's design point will be on the 'turbocharger-
147 engine' system's maximum efficiency point.

148 **2. Methods**

149 In this section, a method for centrifugal compressor design of automotive
150 turbocharger, which does not require much input other than engine operating data, is
151 explained. The method contains the steps of preliminary analysis, throughflow analysis,
152 optimization, and CFD analysis, respectively. These steps and their related settings are
153 explained in detail. In addition, the CFD model, which is a part of this method, has been
154 validated against a centrifugal compressor with a known performance map and steps
155 related to it are presented.

156 **2.1. The Method of Matching a Turbocharger and an Engine**

157 A turbocharger and an engine can be matched at a part or maximum speed of the
158 engine. When the turbocharger and the engine are matched at maximum speed, the

159 turbine's mass flow rate decreases as the engine speed reduces. The power produced by
160 the turbine decreases under this condition. Therefore, the pressure rise generated by the
161 compressor falls, reducing the engine power and torque. If the turbocharger and the
162 engine are matched at a part speed, more turbine power is generated, and the pressure
163 rise across the compressor is higher at the matching engine speed. However, at engine
164 speeds above the matching speed, the boost of the compressor must be limited [7]. The
165 boost limitation can be done by a wastegate or a variable nozzle turbine geometry. In
166 passenger car and light commercial vehicle applications, the engine and the turbocharger
167 are matched at a part speed. On the other hand, in heavy commercial vehicle applications,
168 the matching is done at maximum speed, and free-floating turbochargers are used.

169 To match a turbocharger and an engine, the engine's operating field in addition to the
170 turbocharger compressor map needs to be known. This field is obtained by running the
171 engine at its idle speed, maximum speed, no engine load, and full engine load conditions,
172 respectively. The intake manifold pressure and the mass flow rate of the charge air data
173 are collected during the engine's operation. The data represents the compressor
174 operation's boundaries, and the compressor operates between these boundaries while
175 mounted on that engine. Therefore, this operation field and the performance map of the
176 centrifugal compressor need to match up with each other. The operating field should
177 comprise the best efficiency region of the compressor map. On the other hand, it should
178 not intersect the surge and the choke lines of the map.

179 While designing a turbocharger from scratch, there is no such compressor map to place
180 the engine operating field. Therefore, the compressor can be designed according to the

181 known engine operating field. This approach makes it possible to efficiently design the
182 compressor, as the compressor map's maximum efficiency region can overlap the engine
183 operating field. In this study, the operating field of the engine was obtained in the first
184 instance. For that purpose, the mass flow rate of the charge air and pressure at the intake
185 manifold were measured at different engine loads. An engine test infrastructure is used
186 to run the engine at specified loads and speeds. The engine test infrastructure comprises
187 an Eddy current dynamometer with 150 kW maximum power and 500 Nm maximum
188 torque capacity. The maximum speed limit of the system is 8,000 rpm. Torque and speed
189 sensitivities of the dynamometer are ± 1.25 Nm and ± 1 rpm, respectively. The engine's
190 charge air can be conditioned from 0 °C to 50 °C, from 10% relative humidity to 90%
191 relative humidity and from -15,000 Pa gauge pressure to 35,000 Pa gauge pressure. The
192 fuel entering the engine can also be conditioned and measured. Additionally, blow-by and
193 exhaust backpressure measurement units are installed in the test infrastructure, as shown
194 in Figure 1.

195 The tested engine is a turbocharged diesel engine with a 1.5-liter displacement volume
196 and produces 65 hp power at its rated speed. The measurements were taken at idle
197 speed, maximum speed, no-load, and full load steady-state operating conditions. The
198 dynamometer tests to obtain the engine operation field included seventy-eight different
199 engine operating points. The range of charge-air mass flow rate is from 0.013 kg/s to 0.085
200 kg/s, and the range of intake manifold pressure is from 101,988 Pa to 211,050 Pa. Figure
201 2 shows the measured engine operation field.

202

203 **2.2. Preliminary Analysis**

204 In this step, the compressor stage's preliminary sizing is performed according to
205 fundamental gas dynamics and Euler turbomachinery equations. There are three
206 preliminary analysis sections as: inducer design, exducer design, and diffuser design. The
207 algorithms for inducer and exducer designs are executed simultaneously to make both
208 inducer and exducer rotate at the same speed. On the other hand, diffuser calculations
209 are made separately.

210 The present method calculates the design value of rotational speed based on the
211 designer's choice of the ratio of inducer tip radius (r_{1t}) to exducer radius (r_2), while most
212 prior algorithms need rotational speed value as an input. While designing a turbocharger
213 compressor from scratch, the designer usually has no idea about the design value of the
214 rotational speed. Therefore, the present method enables the user to find the correct
215 design rotational speed value without requiring the designer's input.

216 Original Equipment Manufacturers generally outsource turbocharger development of
217 their internal combustion engine projects to turbocharger suppliers as a specialization-
218 required process. While giving full responsibility to suppliers makes it easier for Original
219 Equipment Manufacturers, this has caused them to act more restrained in terms of
220 engine-specific turbocharger design. The reason for that is turbocharger suppliers often
221 offer off-the-shelf products to Original Equipment Manufacturers as is or with minor
222 modifications, rather than creating tailor-made engine-specific designs. The presented
223 design optimization approach enables Original Equipment Manufacturers to size their
224 engine-specific turbochargers in-house.

225 **2.2.1. Inducer Design**

226 The first step in the preliminary analysis is the inducer's design. The inducer's design
227 objective is to obtain the minimum tip relative velocity required to pass the flow. The
228 inducer design algorithm's inputs are total inlet pressure, inlet total temperature, and
229 mass flow rate. The designer also has a few design choices: inlet absolute flow angle (α_1)
230 and the ratio of inducer hub radius to inducer tip radius (r_{1h}/r_{1t}). For this study, the inlet
231 absolute flow angle (α_1) was taken 0° as there is no inlet guide vane mechanism before
232 the impeller inlet. Hub-tip ratio (r_{1h}/r_{1t}) was chosen 0.5 as the recommended range for
233 this ratio is 0.4-0.6 [13]. The inducer design process starts with estimating the meridional
234 component of absolute inlet velocity (C_{m1}), then other parameters are calculated:

$$C_{\theta 1} = C_{m1} \tan \alpha_1 \quad (1)$$

$$C_1 = (C_{m1}^2 + C_{\theta 1}^2)^{1/2} \quad (2)$$

$$T_1 = T_{00} - (C_1^2 / 2C_p) \quad (3)$$

$$M_1 = C_1 / (kRT_1)^{1/2} \quad (4)$$

$$p_1 = p_{00} (T_1 / T_{00})^{k/(k-1)} \quad (5)$$

$$\rho_1 = p_1 / (RT_1) \quad (6)$$

$$A_1 = \dot{m} / (\rho_1 C_{m1} (1 - B_1)) \quad (7)$$

$$r_{1t} = (A_1 / (\pi(1 - (r_{1h}/r_{1t})^2)))^{1/2} \quad (8)$$

$$U_{1t} = (2\pi r_{1t} N) / 60 \quad (9)$$

$$W_{1t} = \left(C_{m1}^2 + (U_{1t}^2 - C_{\theta 1}^2) \right)^{1/2} \quad (10)$$

235 Inlet absolute velocity (C_{m1}) is iterated until the minimum inlet relative tip velocity
236 (W_{1t}) is reached.

237 **2.2.2. Exducer Design**

238 Together with the inducer analysis, the calculation simultaneously proceeds with
239 determining exducer dimensions, flow state, and velocities. The exducer design
240 algorithm's inputs are inlet total pressure, inlet total temperature, the pressure ratio of
241 the stage, and mass flow rate. The designer also has a few design choices: the ratio of
242 tangential and meridional components of absolute velocity at the impeller exit (λ_2) and
243 blade angle at the impeller exit (β_{2b}). The exducer design process starts with estimating
244 the compressor stage efficiency (η_{stage}), then other parameters are calculated:

$$\Delta h_{0s} = (kRT_{00}/(k - 1)) \left(pr_{stage}^{(k-1)/k} - 1 \right) \quad (11)$$

$$W_x = \Delta h_0 = \Delta h_{0s}/\eta_{stage} \quad (12)$$

$$T_{02} = T_{00} + (\Delta h_0 (k - 1)/kR) \quad (13)$$

$$U_2 = ((U_1 C_{\theta 1} + W_x)/\mu)^{1/2} \quad (14)$$

$$D_2 = (60U_2)/(\pi N) \quad (15)$$

$$C_{\theta 2} = \mu U_2 \quad (16)$$

$$C_{m2} = C_{\theta 2}/\lambda_2 \quad (17)$$

$$T_2 = T_{02} - ((k - 1)(C_{\theta 2}^2 + C_{m2}^2)/2kR) \quad (18)$$

$$p_{02}/p_{00} = (((k - 1)(W_x \eta_{rotor})/(kRT_{00})) + 1)^{k/(k-1)} \quad (19)$$

$$p_{02}/p_2 = (T_{02}/T_2)^{k/(k-1)} \quad (20)$$

$$\rho_2 = p_2/RT_2 \quad (21)$$

$$A_2 = \dot{m}/\rho_2 C_{m2} \quad (22)$$

$$b_2 = A_2/\pi D_2 \quad (23)$$

$$p_5 = p_2 + C_{pD}(p_{02} - p_2) \quad (24)$$

$$\eta_{stage} = ((p_5/p_{00})^{(k-1)/k} - 1)/((T_{02}/T_{00}) - 1) \quad (25)$$

245 Compressor stage efficiency (η_{stage}) is iterated until the ratio of static pressure at
246 diffuser outlet to inlet total pressure (p_5/p_{00}) converges to the pressure ratio of the stage
247 (pr_{stage}). Both inducer and exducer algorithms are solved inside the same iteration loop.
248 The reason for that is the rotational speed is not known before starting the impeller
249 design. A relatively low rotational speed is estimated at the beginning of the run. It is
250 increased until the ratio of inducer tip radius (r_{1t}) to exducer radius (r_2) converges to the
251 desired value. It is recommended by [13] that this value should be in the range of 0.45-
252 0.6. In this study, the ratio of inducer tip radius (r_{1t}) to exducer radius (r_2) was chosen 0.5.
253 Figure 3 shows the process flow chart for the preliminary design algorithm of the
254 turbocharger centrifugal compressor impeller.

255 **2.2.3. Diffuser Design**

256 The final stage in the preliminary design of the centrifugal compressor is the design of
257 the diffuser. Commonly, automotive turbochargers use vaneless diffusers. The vaneless
258 diffuser consists of two parallel or almost parallel walls that form a passage. Therefore,
259 the vaneless diffusers are divided into two: unpinched and pinched (reduced area). In this
260 study, the calculation method for the unpinched type of vaneless diffuser is presented.
261 The preliminary analysis calculations of vaneless diffusers are based on the conservation
262 of mass and momentum equations [27].

263 In this study, the vaneless diffuser design process starts with assuming that there is not
264 any change in total pressure and total temperature values throughout the diffuser, then
265 the other parameters are calculated:

$$p_{05} = p_{02} \quad (26)$$

$$M_5 = \left((2/(k-1)) \left((p_{05}/p_5)^{(k-1)/k} - 1 \right) \right)^{1/2} \quad (27)$$

$$T_{05} = T_{02} \quad (28)$$

$$T_5 = T_{05} / \left(1 + \left(((k-1)/2) + M_5^2 \right) \right) \quad (29)$$

$$C_5 = M_5 (kRT_5)^{1/2} \quad (30)$$

$$\rho_5 = p_5 / RT_5 \quad (31)$$

$$b_5 = b_2 \quad (32)$$

$$r_5 = \left(\left((\dot{m}^2 / 4\pi^2 b_5^2 \rho_5^2) + C_{\theta 2}^2 r_2^2 \right) / C_5^2 \right)^{1/2} \quad (33)$$

266 In the end, main dimensional parameters like inducer hub radius (r_{1h}), inducer tip
267 radius (r_{1t}), exducer radius (r_2), exducer blade height (b_2), diffuser diameter (r_5), and
268 diffuser height (b_5) are obtained. These values are used as input in the throughflow
269 analysis.

270 **2.3. Rotor Geometry via Throughflow Analysis**

271 In this step, the parametric 3D rotor geometry of the centrifugal compressor is created
272 in a Computer-Aided Design (CAD) software using the basic rotor dimensions obtained in
273 the *Preliminary Analysis* subsection. The user should start by drawing a 2D meridional
274 sketch of the compressor in the meridional plane to create a 3D centrifugal compressor
275 geometry from scratch. There should be seven different lines and curves in the 2D view
276 of a centrifugal compressor with splitter blades. These lines and curves are the inlet line
277 of the flow domain, outlet line of the flow domain, hub curve, shroud curve, main blade
278 leading edge curve, main blade trailing edge curve, and splitter blade leading edge curve.

279 There is no need to create a separate curve for the trailing edge of the splitter blade as
280 the trailing edge of the main blade overlaps with the splitter trailing edge in the
281 meridional plane. Therefore, both edges can be represented by a single curve. Figure 4
282 shows the 2D meridional sketch of the centrifugal compressor.

283 All seven lines and curves are created parametrically to recreate the geometry in the
284 optimization phase automatically. In this study, twenty-one drawing parameters were
285 utilized to draw seven sketches automatically. Some of these are independent
286 parameters, while the others are dependent parameters, and they are functions of
287 independent parameters. Dependent parameters change automatically when related
288 independent parameters change. One of the independent parameters in the meridional
289 sketch is also used as an optimization parameter, which means it is the input parameter
290 for geometry optimization. The axial distance between the main blade leading edge and
291 the hub end of the trailing edge (rotor height) is the first optimization parameter. The
292 reason for choosing the rotor height as the optimization parameter is that this parameter
293 cannot be found by the preliminary calculation. Therefore, the value of this parameter is
294 obtained by the optimization study.

295 After creating the meridional sketch, 3D geometries of the main and splitter blades are
296 formed. The thicknesses of the main and splitter blades are automatically determined in
297 the preliminary analysis code as a function of the rotor outlet diameter and then
298 transferred to the CAD software. The number of blades must be entered into the software
299 to generate the main blade. The number of blades is obtained by the definition of the
300 Wiesner slip factor correlation [28]. The slip factor is the measure of slip velocity (C_{slip}),

301 which represents the difference between the exit flow angle (β_2) and the blade angle (β_{2b}).

302 The number of main (Z_{mb}) and splitter blades (Z_{sb}) is calculated as follows:

$$\sigma = \mu(1 - (\tan \beta_{2b} / \lambda_2)) \quad (34)$$

$$Z_{rotor} = ((1 - \cos \beta_{2b}^{1/2}) / \sigma)^{10/7} \quad (35)$$

$$Z_{mb} = Z_{sb} = Z_{rotor}/2 \quad (36)$$

303 Besides the number of blades, theta (ϑ), and beta (β) angle at the leading and trailing
304 edges of the main blade must be defined. Beta (β) angles are calculated during the
305 preliminary analysis phase as follows:

$$\beta_{1h} = \tan^{-1}((C_{\theta 1} - U_{1h}) / C_{m1}) \quad (37)$$

$$\beta_{1t} = \tan^{-1}((C_{\theta 1} - U_{1t}) / C_{m1}) \quad (38)$$

$$\beta_2 = \tan^{-1}((C_{\theta 2} - U_2) / C_{m2}) \quad (39)$$

306 Therefore, the computed values of beta (β) angles are entered into the software as
307 independent parameters. On the other hand, theta (ϑ) angle distribution throughout the
308 meridional section can be determined by parameterizing the leading and trailing edge
309 values. Theta (ϑ) angle value at the trailing edge is set to 0°. On the other hand, the value
310 for the leading edge is defined as an optimization parameter to obtain the optimum rotor
311 geometry. Likewise the rotor height, the theta (ϑ) angle parameter cannot be found by
312 the preliminary calculation. Therefore, the value of this parameter is also obtained by
313 optimization. Consequently, we have two optimization parameters, rotor height, and
314 leading edge theta (ϑ) angle. Figure 5 shows the optimization parameters on the
315 generated parameterized 3D rotor geometry.

316 Created rotor geometry is then transferred to a 2D throughflow solver. Vista TF
317 throughflow solver was used in this study. Vista TF solves inviscid Navier-Stokes equations
318 in a 2D meridional plane and enables the designer to perform a quick analysis to observe
319 the essential flow characteristics before a 3D CFD analysis. Despite giving 2D flow results,
320 the throughflow solver uses 3D rotor geometry to obtain the meridional flow field from
321 it. In addition to the geometry file, rotational direction of the machine, the rotational
322 speed of the design point, mass flow rate of the design point, inlet total pressure, inlet
323 total temperature, and inlet swirl angle values are required. The solver outputs 2D
324 meridional distribution of several flow parameters like pressure, temperature, velocity
325 components, and Mach number. Efficiency and pressure ratio values of the rotor are also
326 calculated by the solver.

327 The output parameter of the optimization study is also defined in the throughflow
328 solver. The total-to-static efficiency of the rotor is defined as the output parameter to
329 obtain the most efficient rotor design at given rotational speed, mass flow rate, and inlet
330 conditions. The maximization of the output parameter is the objective function of this
331 optimization problem.

332 **2.4. Design Optimization**

333 The next step in the current methodology is the optimization of the created 3D rotor
334 geometry based on the throughflow analysis results to obtain the maximum possible
335 total-to-static efficiency at the design point. The optimization problem dealt with in this
336 study is a multivariable non-linear optimization problem. Several optimization techniques

337 were used and compared to find the most appropriate method. The response surface
338 based optimization (RSO) available in [29, 30] was the first method used in this study.
339 Following the RSO, four other optimization methods to find the most suitable method
340 were employed as follows:

- 341 • Response surface based optimization (RSO)
342 • Non-linear programming based on quasi-Newton approach (NLPQN)
343 • Non-linear programming using the derivative-free method (NLPDF)
344 • Pattern search based optimization (PS)
345 • Genetic algorithm (GA)

346 **2.4.1. Response Surface Optimization (RSO)**

347 The RSO method consists of three consecutive steps: Design of Experiments (DoE),
348 Response Surface, and Optimization. In the DoE phase, a representative set of data is
349 collected to create a Response Surface whose accuracy depends on the DoE scheme and
350 the number of calculated design points. There are several DoE schemes available. In this
351 study the Central Composite Design scheme [29, 31] was used. The results of the DoE
352 study in the throughflow analysis step are used to fit a surface for rotor total-to-static
353 efficiency as a function of two optimization parameters: rotor height and leading edge
354 theta (ϑ) angle. In this study, a thin-plate spline method was used to fit a surface to rotor
355 total-static efficiency. The created surface, or function i.e., is the negative of the objective
356 function to be minimized by the solvers.

357 Response Surface is an approximation model function that describes output
358 parameters in terms of input parameters. The Response Surface provides approximate
359 values of the output parameters without the need to obtain a complete solution. There
360 are several Response Surface types available. This study employed the Genetic
361 Aggregation [29] with the Auto-Refinement method.

362 In the Optimization step, the optimization objectives and constraints are defined to
363 seek the optimum geometry. The non-linear programming by quadratic Lagrangian
364 (NLPQL) method was used in this study. NLPQL is a gradient-based single-objective
365 optimization technique that is based on quasi-Newton methods and is convenient for
366 local optimization [29, 32]. While being accurate and fast, NLPQL seeks local optima. Two
367 setting parameters need to be specified for the NLPQL method. These are *Allowable*
368 *Convergence Percentage* and *Derivative Approximation*. *Allowable Convergence*
369 *Percentage* is the convergence tolerance of the NLPQL method. Despite a smaller
370 *Allowable Convergence Percentage* value requires more iterations and decelerates the
371 process, the solution will be more accurate. *Derivative Approximation* determines the
372 calculation method of the objective function gradient. In this study, *Allowable*
373 *Convergence Percentage* and *Derivative Approximation* parameters were set to 10^{-8}
374 (default value is 10^{-6}) and *Central Difference*, respectively.

375 **2.4.2. Non-linear Programming Based on Quasi-Newton Approach (NLPQN)**

376 This optimization approach contains a non-linear programming solver that finds the
377 minimum of an unconstrained multivariable objective function. Gradient methods are

378 more efficient if the function is continuous in its first derivative. Higher-order approaches,
379 such as Newton's method, are really useful only when second-order information is quickly
380 obtained since second-order information is computationally costly. Gradient techniques
381 make use of information about the slope of the function to steer the search towards the
382 direction in which the minimum is believed to exist. The quasi-Newton technique is the
383 most popular of the approaches that employ gradient information. At each iteration,
384 these approaches build curvature information in order to design a quadratic model
385 problem [33].

386 **2.4.3. Non-linear Programming Using the Derivative-Free Method (NLPDF)**

387 This non-linear programming method finds the minimum of an unconstrained
388 multivariable objective function using the derivative-free method. The method uses the
389 Nelder-Mead algorithm as described by Lagarias et al. [34]. For n -dimensional vectors x ,
390 this technique uses a simplex of $n+1$ points. By adding 5% of each component $x_0(i)$ to x_0 ,
391 the method first creates a simplex around the original estimate x_0 . In addition to x_0 , the
392 method employs these n vectors as members of the simplex. The method then repeatedly
393 updates the simplex [33].

394 **2.4.4. Pattern Search Based Optimization (PS)**

395 This optimization approach addresses problems that do not need knowledge of the
396 objective function's gradient. Unlike more traditional optimization methods, which search
397 for an optimal point using information about the gradient or higher derivatives, the PS

398 algorithm searches a set of points surrounding the current point, looking for one where
399 the objective function's value is less than the value at the current point. At each step, the
400 algorithm looks for a collection of points (mesh) that surrounds the current point, the
401 point calculated in the preceding step. The mesh is constructed by multiplying the current
402 point by a scalar multiple of vectors called a pattern. If the PS algorithm discovers a
403 position in the mesh that improves the objective function at the current point, the new
404 point becomes the current point in the next step [33, 35].

405 **2.4.5. Genetic Algorithm (GA)**

406 This method solves smooth or non-smooth optimization problems which can be either
407 constrained or unconstrained. It is a population-based algorithm that randomly selects
408 candidates from the present population and uses them as origins to produce the new
409 candidates for the upcoming generation. The population converges to an optimal solution
410 after consecutive generations. In two significant aspects, the GA is distinct from a
411 standard, derivative-based optimization method. To begin, each iteration of the GA
412 creates a population of points. The population's best point approaches an ideal solution.
413 By contrast, the classical method generates a single point every iteration. The sequence
414 of points is getting closer to an ideal solution. Second, a GA determines the next
415 population via calculation using random number generators. Conversely, a classical
416 algorithm uses a deterministic calculation to determine the next point in the sequence.
417 The GA can be used to tackle a range of optimization problems that are unsuitable for

418 typical optimization techniques, such as those with a discontinuous, non-differentiable,
419 stochastic, or highly non-linear objective function [35].

420 The overall procedure of the methods mentioned above is the same, and it starts with
421 the creation of the objective function in the required format. The process continues with
422 the specific settings of the solvers. These settings are mainly related to how the methods
423 converge to the optimum solution. All methods but GA need an initial point to start the
424 optimization. In this study, optimum design points were obtained with these methods
425 compared with each other.

426 **2.5. CFD Analysis**

427 A 3D CFD analysis can be carried out to verify the performance once the centrifugal
428 compressor's dimensions and angles are determined via preliminary and throughflow
429 studies. The solution domain for the CFD analysis was created using ANSYS TurboGrid,
430 which is a mesh generation software used for turbomachinery geometries. It enables
431 users to create high-quality meshes even for complex geometries rapidly.

432 The software has a typical workflow that contains geometry import, topology
433 generation, mesh generation, and mesh analysis. The most critical step in the TurboGrid
434 workflow is topology generation. Topology is the formation of blocks, and it is used as a
435 framework for positioning the mesh elements. The mesh generation software has
436 Automated Topology and Mesh feature, enabling the user to create a high-quality
437 anisotropic hexahedral mesh quickly. There are two main methods to specify the mesh
438 size in the domain in the software. These are Target Passage Mesh Size and Global Size

439 Factor, respectively. The Target Passage Mesh Size method was used with 2,000,000 node
440 counts in the flow passage. An Edge Refinement Factor was used as the Boundary Layer
441 Refinement Control method, and the factor was set to 5. The Target Maximum Expansion
442 Rate option was selected to prevent a sudden expansion of the mesh size across the flow
443 domain, and it was set to 1.2 for both passage, inlet, and outlet regions. Finally, the Near
444 Wall Element Size Specification method was selected as y^+ , and Reynolds Number was
445 calculated based on the inlet properties and the relative velocity at the meanline inlet.
446 The meridional length of the chord was used as a characteristic length.

$$Re = W_{2,meanline}L_{chord}/v_2 \quad (40)$$

447 The third step in the workflow is the mesh quality analysis done by evaluating the
448 statistics related to mesh quality like Minimum Face Angle, Maximum Face Angle,
449 Maximum Element Volume Ratio, Maximum Edge Length Ratio, etc. One can
450 acknowledge the quality and the conformity of the generated mesh if there is no warning
451 regarding these parameters. Figure 6 shows the generated mesh for the present solution
452 domain.

453 The CFD solver for this work is ANSYS CFX, a solver specializing in turbomachinery
454 components, including pumps, fans, compressors, and turbines [36]. The analysis type
455 was set to a steady state as this analysis aims to observe the centrifugal compressor's
456 performance at a continuous flow regime. The rotor region in the flow domain was
457 defined as a rotating component, and the analysis speed was set in terms of revolutions
458 per minute. The Frozen Rotor method was used to model the interaction between the
459 rotating (rotor) and stationary (vaneless diffuser) frames.

460 The next step in the setup phase is selecting the fluid and models for heat transfer and
461 turbulence. Air Ideal Gas was established as fluid to activate compressible flow modeling.
462 Heat transfer and turbulence models were set to Total Energy and Shear Stress Transport
463 (SST), respectively. The Total Energy option contains kinetic energy effects, unlike the
464 Thermal Energy option. This difference makes the Total Energy option is the appropriate
465 option for compressible flows. The SST turbulence model overcomes the drawbacks of k -
466 ε and $k-\omega$ models and blends between the two models based on the distance from the
467 walls [37]. The automatic wall function option is used with the SST model. It is an
468 improved near-wall treatment model which shifts smoothly from a conventional low-Re
469 formulation on fine grids to a log-wall function formulation on coarser meshes. This
470 automated switching of the wall function formulation eliminates the grid resolution
471 constraints associated with typical low-Re number turbulence models. It is shown in [38]
472 that the SST model with the automatic wall function gives similar results for the values of
473 y^+ ranging from 0.1 to 100 in the same rotating machinery cases. In the present study, the
474 near-wall mesh sizing was made so that the maximum y^+ value on the walls is 25.
475 The total pressure inlet and mass flow outlet options were selected to specify inflow
476 and outflow boundary options. This couple, as boundary conditions, is the essential
477 option to obtain pressure values at the outlet. Thermal boundary conditions of all walls
478 in the flow passage including hub, shroud, and blade surfaces were set as Dirichlet
479 boundary condition. The static temperature value at the impeller outlet calculated in the
480 *Preliminary Analysis* subsection was entered as a boundary condition for all walls.

481 Advection Scheme and Turbulence Numerics were both set to High-Resolution option.
482 Conservative Auto Timescale was used with the Maximum Timescale option, and the
483 maximum value for timescale was set to $1/\omega$ value in terms of seconds. Residual Type and
484 Residual Target were set to MAX and 0.0001, respectively. The Conservation Target
485 option was selected, and the value for this option was set at 0.01 to define a target for
486 the global imbalances. Finally, the convergency monitors were created to track the values
487 of interest as the solver runs. These monitors are outlet total pressure, outlet pressure,
488 outlet total temperature, and outlet temperature.

489 **2.6 Validation of the CFD Model**

490 To validate the CFD model setup and its parameters described in the previous section,
491 a similar turbocharger with a known compressor performance map is taken as a
492 reference. The turbocharger used for validation belongs to a 7.5-liter heavy-duty vehicle
493 engine which has 1,450 Nm and 265 kW maximum torque and maximum power values,
494 respectively. The compressor performance map of the turbocharger was provided by the
495 company mentioned in the *Acknowledgment* section that funded this study. The map had
496 been created by the company as part of a previous project and it was shared with the
497 authors for the validation of the CFD model. Figure 7 shows the compressor performance
498 of the reference turbocharger.

499 3D CAD data of the reference compressor was used to obtain the flow geometry which
500 is required in mesh generation and CFD model setup steps, respectively. The reference
501 compressor has seven main and seven splitter blades. The inlet hub, inlet shroud, and

502 outlet radii are 10.8 mm, 31.75 mm, and 46 mm, respectively. The blade height at the
503 rotor outlet is 4.7 mm, and the thickness of the blades is 0.5 mm. Figure 8 presents the
504 reference compressor and the CAD model of the reference compressor.

505 Three different meshes were generated from the flow geometry of the reference
506 compressor for mesh sensitivity study. The topology and mesh setup for these three
507 meshes are the same as explained in the *CFD Analysis* subsection. The difference between
508 the meshes is the node count of the passage region. Node counts were set to 1,250,000,
509 2,500,000, and 3,750,000 for coarse, medium, and fine meshes, respectively. As a result,
510 the node counts of these three meshes became 1,376,826, 2,692,542, and 3,971,185.

511 Figure 9 shows the generated meshes for the mesh sensitivity study.

512 Rotational speed and mass flow rate data from the performance map were used in the
513 CFD model as domain rotational speed and outlet boundary conditions, respectively. Inlet
514 boundary condition, which is total pressure inlet, was set to atmospheric pressure for all
515 cases. Fifty-one cases were prepared for each mesh, and a total of one hundred and fifty-
516 three cases were solved in the CFD solver with the settings explained in the *CFD Analysis*
517 subsection. All cases were converged as maximum values of all residuals dropped below
518 0.0001, and the monitors for values of interests remained unchanged before the
519 completion of each run.

520 The reference compressor's CFD results demonstrate that reasonable mesh
521 independence is obtained as the difference between the effects of medium and fine
522 meshes is tolerably small. The minimum and maximum deviations percentage range of
523 the CFD results from the total-to-static pressure ratio map data are 6.1-11.2%, 2.6-6.9%,

524 and 1.2-4.2% for coarse, medium, and fine meshes, respectively. The computational
525 results do not change significantly as the node count of the passage region goes beyond
526 2,500,000. Figure 10 shows the total-to-static pressure ratio CFD results of the three
527 meshes and the map data.

528 The minimum and maximum deviations percentage range of the CFD results from the
529 total-to-static efficiency map data are 5.9-10.4%, 2.4-6.7%, and 1.1-3.9% for coarse,
530 medium, and fine meshes, respectively. Figure 11 shows the total-to-static efficiency CFD
531 results of the three meshes and the map data.

532 **3. Results**

533 An exemplary compressor design was carried out using the method described in the
534 previous section. In this study, a centrifugal compressor design has been made from
535 scratch for the internal combustion engine whose operation map is given in Figure 2.

536 **3.1. Preliminary Analysis Results**

537 The engine operation field is divided into linearly spaced separate small regions. The
538 corner points of these regions are used as input conditions for the preliminary analysis.
539 Every point represents a mass flow rate and outlet total pressure couple. The couple that
540 gives the highest compressor efficiency forms the design point of the compressor. In other
541 words, the compressor will provide its best performance if it is designed based on these
542 mass flow rates and total pressure values. Figure 12 shows the engine operation field
543 marked by total-to-static efficiency values obtained from the preliminary analysis code.

544 The white dot in the figure represents the design mass flow rate and outlet total pressure
545 couple chosen in the preliminary analysis.

546 Although there appears to be a difference of only 0.02 between the maximum and
547 minimum efficient design points, significant differences in off-design performances are
548 expected as these points only represent the best points in their own performance maps.

549 To check this, the centrifugal compressor performance maps of the maximum and
550 minimum design points were created and compared with each other. The method
551 presented by Casey and Robinson [39] was used to estimate the performance maps of the
552 maximum and minimum design points. In this method, the performance of the centrifugal
553 compressor map is based on four non-dimensional parameters (flow coefficient, work
554 coefficient, tip-speed Mach number, and efficiency) composed of physically-based
555 algebraic equations without requiring much knowledge about the geometry itself. It has
556 been revealed that the efficiency and pressure ratio values of the turbochargers with
557 vaneless diffusers can be estimated with a maximum deviation of 2% by this method. The
558 details of the method can be found in the aforementioned reference [39] and will not be
559 mentioned within the scope of this article. The performance maps of the minimum and
560 maximum design points are given in Figure 13 comparatively.

561 First of all, the compressor design created with the minimum design point will provide
562 considerably lower pressure ratios than the design created with the maximum design
563 point. At their maximum efficiency points, they provide around 1.0065 and 2.08 total-to
564 static pressure ratios, respectively. Also, as can be seen from the figure that the maximum
565 efficiency region of the minimum design point's performance map is much smaller than

566 the maximum efficiency region of the maximum design point's performance map. This
567 indicates that the compressor design with the maximum design point exhibits much
568 better off-design performance. In addition, the centrifugal compressor to be produced
569 using the minimum design point will have to operate at very high speeds, these values do
570 not seem possible with the existing turbocharger bearing technologies. Considering all of
571 these, it appears that the selection of the design point in the preliminary analysis step is
572 quite critical.

573 The highest efficiency is observed at (0.0583 kg/s, 211,050 Pa) point which is shown as
574 a white circular symbol in Figure 13 (b). Table 1 presents the basic preliminary analysis
575 results of that point.

576 **3.2. Throughflow Analysis Results**

577 The basic dimensions obtained from the preliminary analysis are transferred to the
578 generated parametric 3D compressor geometry, which is presented in the *Rotor*
579 *Geometry via Throughflow Analysis* subsection. In addition to the main dimensions, the
580 rotational direction of the machine, the rotational speed of the design point, the mass
581 flow rate of the design point, inlet total pressure, inlet total temperature, and inlet swirl
582 angle values are also entered into the throughflow model.

583 Since the design optimization study is carried out depending on the throughflow
584 analysis results, the throughflow analysis results shared in this section belong to the final
585 design obtained as a result of the optimization study shared in the *Design Optimization*

586 *Results* subsection. Figure 14 reveals the throughflow analysis results of the optimum
587 design for total pressure, static pressure, total temperature, and static temperature.

588 Table 2 lists a comparison of the preliminary and throughflow analysis results at the
589 stage exit. The preliminary and throughflow analysis results matched up reasonably well
590 with each other.

591 The throughflow analysis results given in Table 2 belong to the rotor geometry created
592 by using the rotor height and the leading edge theta (ϑ) angle parameters obtained as a
593 result of the optimization study described in the next subsection.

594 **3.3. Design Optimization Results**

595 The optimization results of RSO, NLPQN, NLPDF, PS and GA methods are shared in this
596 section. The optimization calculations were performed on a 3.10 GHz Intel Xeon processor
597 with 10 cores. The design optimization study started with the solution of the DoE points.
598 For the rotor height and leading edge theta (ϑ) angle, 11 values were taken in the ranges
599 of 15 mm-45 mm and 15°-75°, respectively, and a total of one hundred and twenty-one
600 different design points were created and solved in the throughflow solver. After the DoE
601 step, a surface was fitted to the experiment points to obtain the total-to-static efficiency
602 as a function of rotor height and leading edge theta (ϑ) angle variables. RSO uses a unique
603 and non-modifiable surface fitting tool. For this reason, while RSO uses its own function,
604 other optimization methods use a separate function created separately. The created
605 total-to-static efficiency function is given in Figure 15.

606 The NLPQL method was used in RSO. The objective type was set to maximize (total-to-
607 static efficiency), and no constraint was applied to the variables and the objective. The
608 result of the NLPQL method is 35.82 mm, 57.16°, and 0.7022 for rotor height, leading edge
609 theta (ϑ), and total-to-static efficiency, respectively. The CPU time spent during the RSO
610 method was 102.6 s.

611 NLPQN, NLPDF, and PS methods require an initial point to solve the optimization
612 problem. Since the user will probably not have a guess as to what an accurate starting
613 point will be, in this study the results of these three methods for four different starting
614 points were obtained. The results of NLPQN, NLPDF, and PS are given in Table 3.

615 The results show that all three methods are dependent on the initial point. In addition,
616 the NLPQN method converges faster than others, while the PS method converges slower
617 but gives better results even with the initial points in which NLPQN and NLPDF converge
618 to lower efficiency values. To show that NLPQN, NLPDF, and PS methods can converge to
619 different values even if they start the calculations from the same initial point, the cases
620 where they start from the (Height: 35 mm, Theta (ϑ): 35°) point in Table 3 are given in
621 Figure 16.

622 On the other hand, GA does not need an initial point to start the calculation. Therefore,
623 it is possible for the user to perform the optimization work correctly without an
624 estimation of the correct initial point. The population size used by the GA method is
625 chosen 50 as the number of variables is 2, as recommended in [35]. The initial population
626 is created by uniform random number generator, within the range set for the variables.
627 The mutation and crossover rates are 0.1 and 0.9, respectively. The result of the GA

628 method is 29.91 mm, 50.76°, and 0.7184 for rotor height, leading edge theta (ϑ), and
629 total-to-static efficiency, respectively. GA created 66 generations to achieve the optimum
630 result. The CPU time spent during the GA method was 122.4 s. Figure 17 shows the best
631 candidate points in all generations of the GA method during converging the solution.

632 **3.4. CFD Analysis Results**

633 The optimized 3D centrifugal geometry was then analyzed in the CFD solver with the
634 settings described in the *CFD Analysis* subsection. Analysis was performed only for the
635 design point. Figure 18 shows 3D CFD analysis results for p_0 and p .

636 A comparison of preliminary, throughflow, and CFD analysis results of the design point
637 is given in Table 4. The values in parentheses represent the percentage deviations from
638 the CFD results. The results matched up with each other very well.

639 It is obvious that the CFD results will be the most realistic among the results of the
640 three analysis types since the CFD results include 3D effects and the CFD model was
641 validated with the test results of a reference centrifugal compressor in the *Validation of*
642 *the CFD Model* subsection. Therefore, when the preliminary and throughflow results are
643 compared with the CFD results, the deviations are 5.2%-3.0%, 5.1%-2.4%, 2.5%-1.4%,
644 2.2%-0.9%, 3.0%-1.4% and 2.7%-2.4% for p_{05} , p_5 , T_{05} , T_5 , M_5 , and η_{ts} , respectively. These
645 deviations show that the current method performs quite well even at the preliminary
646 level.

647

648 **4. Conclusions and Future Work**

649 While designing a turbocharger from scratch, there is usually no compressor map
650 already matched to the specific engine operating field. The procedures defined in this
651 investigation make it possible to efficiently design a turbocharger compressor such that
652 its maximum efficiency region can overlap the engine operating field.

653 The method presented in this article is based on first principles, straightforward, and
654 reasonably accurate. The current method's required inputs are charge-air mass flow rate
655 and intake manifold pressure values of the engine under different load and speed
656 conditions. The preliminary analysis forms the basic stage dimensions and obtains basic
657 flow properties. The preliminary sizing method presented in this study differs from the
658 existing sizing algorithms as the method does not perform sizing calculations based on
659 the design rotational speed value defined by the user. The algorithm calculates the
660 optimum design rotational speed value based on the engine performance map and design
661 considerations.

662 The preliminary analysis calculates only the basic geometrical features. On the other
663 hand, features like rotor height and leading edge theta (ϑ) can only be determined by a
664 proper optimization study. Therefore, an optimization study follows the preliminary
665 investigation to find the optimum compressor geometry by performing throughflow
666 analyses. The compressor geometry is optimized to obtain the maximum possible total-
667 to-static efficiency by finding the optimum values for rotor height and leading edge theta
668 (ϑ). After trying five different optimization methods, it has been found that GA is the most
669 suitable method for such a turbomachinery design optimization problem.

670 The final geometry is then transferred to a CFD pre-processor and CFD solver to create
671 a 3D mesh and complete a 3D CFD analysis, respectively. As indicated in Table 4, the
672 results from all three steps match up with each other. The present study shows that
673 preliminary sizing followed by a well-built throughflow analysis based optimization
674 eliminates the need for a fully parametric 3D CFD-based design.

675 The CFD analysis part of this work can be a guide for all who want to run CFD analysis
676 for centrifugal machinery regardless of it is a turbocharger compressor or not. The
677 workflow from mesh generation to model run was described broadly by declaring all
678 selected sub-models and used parameters. The CFD analysis was validated against a
679 reference compressor performance map containing fifty-one data points at seven
680 speedlines. The results show that the minimum and maximum deviations percentage
681 range of the CFD results from the total-to-static pressure ratio map data is 1.2-4.2% for
682 the fine mesh.

683 The current design strategy can reduce engine emissions because of these well-
684 matched turbochargers. The engine cycle efficiency and combustion characteristics can
685 also be improved with better-matched turbochargers over a wide operational range.
686 Besides the performance and environmental effects, the present method will also shorten
687 the design sequence by eliminating the trial-and-error loops inherent while matching the
688 engine with an off-the-shelf turbocharger in conventional design efforts.

689 Adding volute design, radial turbine design and FEA steps to the overall design effort
690 can improve the present method. The user can also design the turbocharger's turbine side

691 and test the operation of both the centrifugal compressor and radial turbine
692 simultaneously.

693 **Acknowledgment**

694 The authors wish to thank Supsan Automotive Components for funding this study by
695 putting its engine test infrastructure at the authors' service and supplying the centrifugal
696 compressor performance map and the test engine.

697 **Nomenclature**

A	= area m^2
B	= boundary layer blockage coefficient
b	= blade height m
C	= absolute velocity m/s
CAD	= Computer-Aided Design
CAE	= Computer-Aided Engineering
CAM	= Computer-Aided Manufacturing
CFD	= Computational Fluid Dynamics
C_p	= specific heat at constant pressure J/kgK
C_{pD}	= diffuser pressure recovery coefficient
D	= diameter m
DoE	= Design of Experiments
FEA	= Finite Element Analysis
GA	= genetic algorithm
h	= specific enthalpy J/kg
k	= ratio of specific heats, turbulent kinetic energy m^2/s^2
L	= length m
LE	= Leading edge
M	= Mach number
\dot{m}	= mass flow rate kg/s
N	= rotational speed rpm
NLPDF	= non-linear programming using the derivative-free method
NLPQL	= non-linear programming by quadratic Lagrangian
NLPQN	= non-linear programming based on quasi-Newton approach
p	= pressure Pa
pr	= pressure ratio
PS	= pattern search based optimization
r	= radius m
R	= gas constant J/kgK
Re	= Reynolds number

RSO	= response surface based optimization
SST	= Shear Stress Transport
T	= temperature K
TE	= Trailing edge
U	= blade speed m/s
W	= relative velocity m/s
W_x	= shaft work J/kg
Z	= number of blades
α	= absolute flow angle $^{\circ}$
β	= relative flow angle $^{\circ}$
Δ	= difference
ε	= dissipation rate m^2/s^3
η	= efficiency
ϑ	= theta angle $^{\circ}$
λ	= swirl parameter
μ	= work coefficient
ν	= kinematic viscosity m^2/s
ρ	= density kg/m^3
σ	= slip factor
ω	= specific dissipation rate s^{-1} , rotational speed s^{-1}

Subscripts

0	= stagnation condition
1	= impeller inlet
2	= impeller exit
3	= diffuser inlet
4	= diffuser throat
5	= diffuser exit
b	= blade property
h	= hub
m	= meridional component
mb	= main blade
s	= isentropic
sb	= splitter blade
t	= tip
ts	= total-to-static
ϑ	= tangential component

698 **References**

- 699 1. Garrett Motion, n.d., "How a Turbo Works – Basic," Accessed December 1, 2021,
700 <https://www.garrettmotion.com/knowledge-center-category/oem/basic/>.
- 701 2. Hiereth, H., and Prenninger, P., 2007, *Charging the Internal Combustion Engine*, Vienna:
702 Springer. <https://doi.org/10.1007/978-3-211-47113-5>.
- 703 3. Watson, N., and Janota, M. S., 1982, *Turbocharging the Internal Combustion Engine*,
704 London: Palgrave. <https://doi.org/10.1007/978-1-349-04024-7>.

- 705 4. Nguyen-Schäfer, H., 2013, *Aero and Vibroacoustics of Automotive Turbochargers*,
706 Berlin: Springer. <https://doi.org/10.1007/978-3-642-35070-2>.
- 707 5. Walsham, B.E., and Winterbone, D.E., 1990, "The Turbocharger," In *Internal*
708 *Combustion Engineering: Science & Technology*, edited by Weaving, J. H., 615-706,
709 Dordrecht: Springer. https://doi.org/10.1007/978-94-009-0749-2_14.
- 710 6. Nguyen-Schäfer, H., 2015, *Rotordynamics of Automotive Turbochargers*, Cham:
711 Springer. <https://doi.org/10.1007/978-3-642-27518-0>.
- 712 7. Baines, N. C., 2005, *Fundamentals of Turbocharging*, Vermont: Concepts ETI.
- 713 8. Cummins, n.d., "Turbocharger History," Accessed December 1, 2021,
714 <http://www.cummins.ru/en/components/turbo-technologies/turbocharger-history>.
- 715 9. BorgWarner, n.d., "Boosting Technologies," Accessed December 1, 2021,
716 <https://www.borgwarner.com/technologies/boosting-technologies>.
- 717 10. Golloc, R., and Merker, G.P., 2005, "Internal Combustion Engine Downsizing," *MTZ Worldwide* 66(2): 20-22. <https://doi.org/10.1007/BF03227737>.
- 719 11. Eriksson, L., Wahlström, J., and Klein, M., 2010, "Physical Modeling of Turbocharged
720 Engines and Parameter Identification," In *Automotive Model Predictive Control*, edited by
721 del Re, L., Allgöwer, F., Glielmo, L., Guardiola, C., and Kolmanovsky, I., 53-71, London:
722 Springer. https://doi.org/10.1007/978-1-84996-071-7_4.
- 723 12. Japikse, D., and Baines, N. C., 1997, *Introduction to Turbomachinery*, Vermont:
724 Concepts ETI.
- 725 13. Japikse, D., 1996, *Centrifugal Compressor Design and Performance*, Vermont:
726 Concepts ETI.
- 727 14. Qiu, X., Fredriksson, C. F., Baines, N. C., and Backlund, M., 2013, "Designing
728 Turbochargers with an Integrated Design System," Proceedings of the ASME Turbo Expo
729 2013: Turbine Technical Conference and Exposition. Volume 5A: Industrial and
730 Cogeneration; Manufacturing Materials and Metallurgy; Marine; Microturbines,
731 Turbochargers, and Small Turbomachines, San Antonio, Texas, June 3-7, 2013, ASME
732 Paper No. V05AT23A017. <https://doi.org/10.1115/GT2013-94894>.
- 733 15. De Bellis, V., Bozza, F., Bevilacqua, M., Bonamassa, G., and Schernus, C., 2013,
734 "Validation of a 1D Compressor Model for Performance Prediction," SAE Technical Paper
735 No. 2013-24-0120. <https://doi.org/10.4271/2013-24-0120>.
- 736 16. Canova, M., Naddeo, M., Liu, Y., Zhou, J., and Wang, Y. Y., 2015, "A Scalable Modeling
737 Approach for the Simulation and Design Optimization of Automotive Turbochargers," SAE
738 Technical Paper No. 2015-01-1288. <https://doi.org/10.4271/2015-01-1288>.

- 739 17. Nasser, S., and Playfoot, B., 1999, "A Turbocharger Selection Computer Model," SAE
740 Technical Paper No. 1999-01-0559. <https://doi.org/10.4271/1999-01-0559>.
- 741 18. Pakle, S., and Jiang, K., 2018, "Design of a High-Performance Centrifugal Compressor
742 with New Surge Margin Improvement Technique for High Speed Turbomachinery,"
743 *Propulsion and Power Research* 7(1): 19-29. <https://doi.org/10.1016/j.jppr.2018.02.004>.
- 744 19. Favaretto, C. F. F., Anderson, M. R., Li, S., and Hu, L., 2018, "Development of a
745 Meanline Model for Preliminary Design of Recirculating Casing Treatment in Turbocharger
746 Compressors," Proceedings of the ASME Turbo Expo 2018: Turbomachinery Technical
747 Conference and Exposition. Volume 8: Microturbines, Turbochargers, and Small
748 Turbomachines; Steam Turbines, Oslo, June 11-15, 2018, ASME Paper No. V008T26A006.
749 <https://doi.org/10.1115/GT2018-75717>.
- 750 20. Dombrovsky, A., 2017, "Synthesis of the 1D Modelling of Turbochargers and Its Effects
751 on Engine Performance Prediction," Ph.D. dissertation, Universitat Politècnica de
752 València, Valencia.
- 753 21. Dehner, R., Selamet, A., Keller, P., and Becker, M., 2010, "Simulation of Mild Surge in
754 a Turbocharger Compression System," SAE Technical Paper No. 2010-01-2142.
755 <https://doi.org/10.4271/2010-01-2142>.
- 756 22. Im, K., 2012, "Development of a Design Method for Centrifugal Compressors," Ph.D.
757 dissertation, Michigan State University, East Lansing, MI.
- 758 23. Schiff, J., 2013, "A Preliminary Design Tool for Radial Compressors," M.Sc. thesis, Lund
759 University, Lund.
- 760 24. Buchman, M., Ramanujan, D., and Winter, A., 2018, "A Method for Turbocharging
761 Single-Cylinder, Four-Stroke Engines," SAE Technical Paper No. 03-11-04-0028.
762 <https://doi.org/10.4271/03-11-04-0028>.
- 763 25. Tsukiyama, T., Yonezawa, K., Iwata, H., and Ishikawa, M., 2015, "Development of New
764 Toyota D-Series Turbocharger for GD Diesel Engine," SAE Technical Paper No. 2015-01-
765 1969. <https://doi.org/10.4271/2015-01-1969>.
- 766 26. Golovan, A., Gritsuk, I., Popeliuk, V., Sherstyuk, O., et al., 2020, "Features of
767 Mathematical Modeling in the Problems of Determining the Power of a Turbocharged
768 Engine According to the Characteristics of the Turbocharger," SAE Technical Paper No. 03-
769 13-01-0001. <https://doi.org/10.4271/03-13-01-0001>.
- 770 27. Japikse, D., and Baines, N. C., 1998, *Diffuser Design Technology*, Vermont: Concepts
771 ETI.
- 772 28. Wiesner, F. J., 1967, "A Review of Slip Factors for Centrifugal Impellers," *ASME J. Eng.*
773 *Power* 89(4): 558-566. <https://doi.org/10.1115/1.3616734>.

- 774 29. ANSYS, 2014, *Design Exploration User's Guide*, Release 15.0, Canonsburg, PA: ANSYS.
- 775 30. Box, G.E.P., and Wilson, K.B., 1951, "On the Experimental Attainment of Optimum
776 Conditions," *Journal of the Royal Statistical Society: Series B (Methodological)* 13(1): 1-38.
777 <https://doi.org/10.1111/j.2517-6161.1951.tb00067.x>.
- 778 31. Montgomery, D. C., 2005, *Design and Analysis of Experiments*, New York: John Wiley
779 & Sons.
- 780 32. Schittkowski, K., 1986, "NLPQL: A Fortran Subroutine Solving Constrained Nonlinear
781 Programming Problems," *Annals of Operations Research* 5(2): 485-500.
782 <https://doi.org/10.1007/BF02022087>.
- 783 33. MATLAB, 2021, "MATLAB Optimization Toolbox™ User's Guide," Revision 9.2,
784 MathWorks Help Center PDF Documentation for Optimization Toolbox, last modified
785 September, 2021, https://www.mathworks.com/help/pdf_doc/optim/optim.pdf.
- 786 34. Lagarias, J. C., Reeds, J. A., Wright, M. H., and Wright., P. E., 1998, "Convergence
787 Properties of the Nelder-Mead Simplex Method in Low Dimensions," *SIAM Journal of
788 Optimization* 9(1): 112–147. <https://doi.org/10.1137/S1052623496303470>.
- 789 35. MATLAB, 2021, "MATLAB Global Optimization Toolbox User's Guide," revision 4.6,
790 MathWorks Help Center PDF Documentation for Optimization Toolbox, last modified
791 September, 2021, https://www.mathworks.com/help/pdf_doc/gads/gads.pdf.
- 792 36. ANSYS, n.d., "Computational Fluid Dynamics (CFD) Software Program Solutions,"
793 Accessed October, 12, 2021, <https://www.ansys.com/products/fluids/ansys-cfx>.
- 794 37. Menter, F. R., 1994, "Two-Equation Eddy-Viscosity Turbulence Models for Engineering
795 Applications," *AIAA Journal* 32(8): 1598-1605. <https://doi.org/10.2514/3.12149>.
- 796 38. Menter, F. R., Ferreira, J. C., and Esch, T., 2003, "The SST Turbulence Model with
797 Improved Wall Treatment for Heat Transfer Predictions in Gas Turbines," Proceedings of
798 the International Gas Turbine Congress 2003, Tokyo, November 2-7, 2003, Gas Turbine
799 Society of Japan (GTSJ) Paper No. IGTC2003-TS-059.
- 800 39. Casey, M., and Robinson, C., 2013, "A Method to Estimate the Performance Map of a
801 Centrifugal Compressor Stage," *ASME J. Turbomach.* 135(2): 021034.
802 <https://doi.org/10.1115/1.4006590>.
- 803
804
805
806
807
808

809

Table Caption List

- Table 1 Preliminary analysis results of the design point
- Table 2 Preliminary and throughflow analysis results of the design point
- Table 3 Results of NLPQN, NLPDF and PS methods
- Table 4 Preliminary, throughflow, and CFD analysis results of the design point

810

Figure Caption List

- Fig. 1 The engine test setup
- Fig. 2 Measured engine operation field
- Fig. 3 Centrifugal compressor impeller preliminary design algorithm
- Fig. 4 Parametric meridional view of the centrifugal compressor
- Fig. 5 Optimization parameters of the parameterized rotor geometry
- Fig. 6 Periodic mesh of the centrifugal compressor flow domain
- Fig. 7 Compressor performance map of the reference turbocharger
- Fig. 8 (a) The reference compressor and (b) its CAD model
- Fig. 9 Three different meshes for the mesh sensitivity: (a) coarse, (b) medium, (c) fine
- Fig. 10 Comparison of total-to-static pressure ratio CFD results and map data
- Fig. 11 Comparison of total-to-static efficiency CFD results and map data
- Fig. 12 Efficiency map of the engine operation field
- Fig. 13 Comparison of the maps of (a) minimum and (b) maximum design points
- Fig. 14 Throughflow analysis results of the optimum design: (a) p_0 , (b) p , (c) T_0 , (d) T
- Fig. 15 Total-to-static efficiency function created from throughflow results
- Fig. 16 Converging to different values via (a) NLPQN, (b) NLPDF and (c) PS methods
- Fig. 17 Genetic algorithm solution
- Fig. 18 3D CFD analysis results of the design point: (a) p_0 , (b) p

811

812

Table 1 Preliminary analysis results of the design point.

Parameter	Impeller Inlet	Impeller Outlet	Diffuser Outlet
p_0 [Pa]	101,325.0	248,301.9	248,301.9
p [Pa]	92,507.9	169,798.4	208,052.4
T_0 [K]	293.2	388.0	388.0
T [K]	285.6	346.5	368.7
ρ [kg/m ³]	1.13	1.71	1.99
M [-]	0.36	0.77	0.51
r_{1h} [mm]	6.78	-	-
r_{1t} [mm]	13.55	-	-
r_2 [mm]	-	27.32	-
b_2 [mm]	-	1.54	-
r_5 [mm]	-	-	38.98
Z_{mb} [-]		8	
N [rpm]		129,000	
β_{1h} [°]	-36.66	-	-
β_{1t} [°]	-56.11	-	-
β_2 [°]	-	-40.60	-
η_{ts} [-]		0.7206	

813

814

815

Table 2 Preliminary and throughflow analysis results of the design point.

Analysis	p_{05} [Pa]	p_5 [Pa]	T_{05} [K]	T_5 [K]	M_5 [-]	η_{ts} [-]
Preliminary	248,301.9	208,052.4	388.0	368.7	0.51	0.7206
Throughflow	243,146.1	202,766.5	383.8	364.2	0.50	0.7184

816

Accepted Manuscript Not Copyedited

817

Table 3 Results of NLPQN, NLPDF, and PS methods.

Method	Initial Point	Iterations / CPU Time	Height	Theta [θ]	Value
NLPQN	25 mm, 35°	12 / 16.4 s	29.93 mm	50.84°	0.7184
	25 mm, 55°	12 / 16.9 s	29.93 mm	50.84°	0.7184
	35 mm, 35°	11 / 13.2 s	35.23 mm	30.82°	0.7080
NLPDF	35 mm, 55°	9 / 12.6 s	36.12 mm	56.57°	0.7025
	25 mm, 35°	46 / 26.3 s	35.23 mm	30.82°	0.7080
	25 mm, 55°	49 / 28.3 s	29.93 mm	50.84°	0.7184
PS	35 mm, 35°	45 / 27.7 s	29.93 mm	50.84°	0.7184
	35 mm, 55°	39 / 25.2 s	36.12 mm	56.57°	0.7025
	25 mm, 35°	66 / 36.4 s	29.93 mm	50.84°	0.7184
PS	25 mm, 55°	58 / 32.8 s	29.93 mm	50.84°	0.7184
	35 mm, 35°	58 / 34.1 s	35.23 mm	30.82°	0.7080
	35 mm, 55°	62 / 35.0 s	29.93 mm	50.84°	0.7184

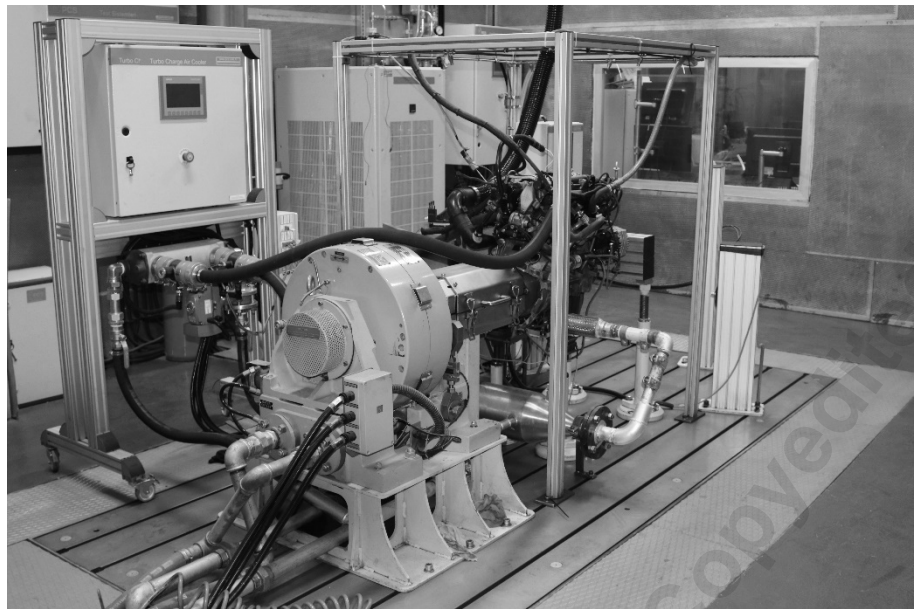
818

819

Table 4 Preliminary, throughflow, and CFD analysis results of the design point.

Analysis	p_{05} [Pa]	p_5 [Pa]	T_{05} [K]	T_5 [K]	M_5 [-]	η_{ts} [-]
Preliminary	248,301.9 (5.2%)	208,052.4 (5.1%)	388.0 (2.5%)	368.7 (2.2%)	0.51 (3.0%)	0.7206 (2.7%)
	243,146.1 (3.0%)	202,766.5 (2.4%)	383.8 (1.4%)	364.2 (0.9%)	0.50 (1.4%)	0.7184 (2.4%)
CFD	236,028.3 (-)	198,013.7 (-)	378.6 (-)	360.8 (-)	0.50 (-)	0.7015 (-)

820



821

Fig. 1 The engine test setup.

822

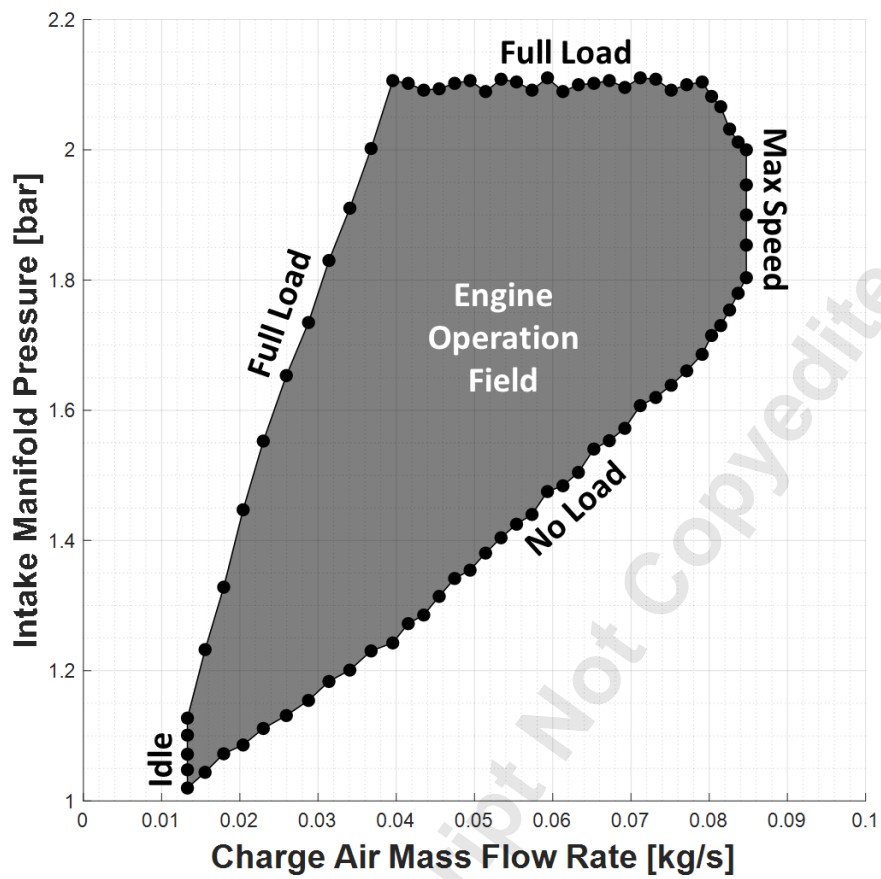


Fig. 2 Measured engine operation field.

823

824

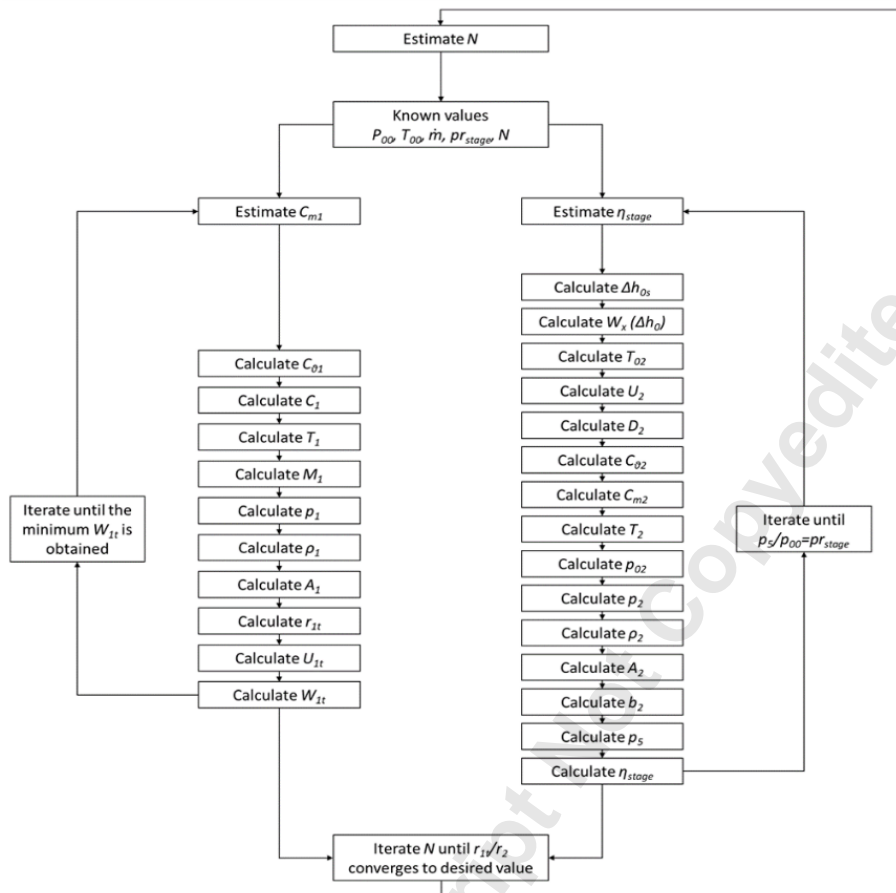


Fig. 3 Centrifugal compressor impeller preliminary design algorithm.

825

826

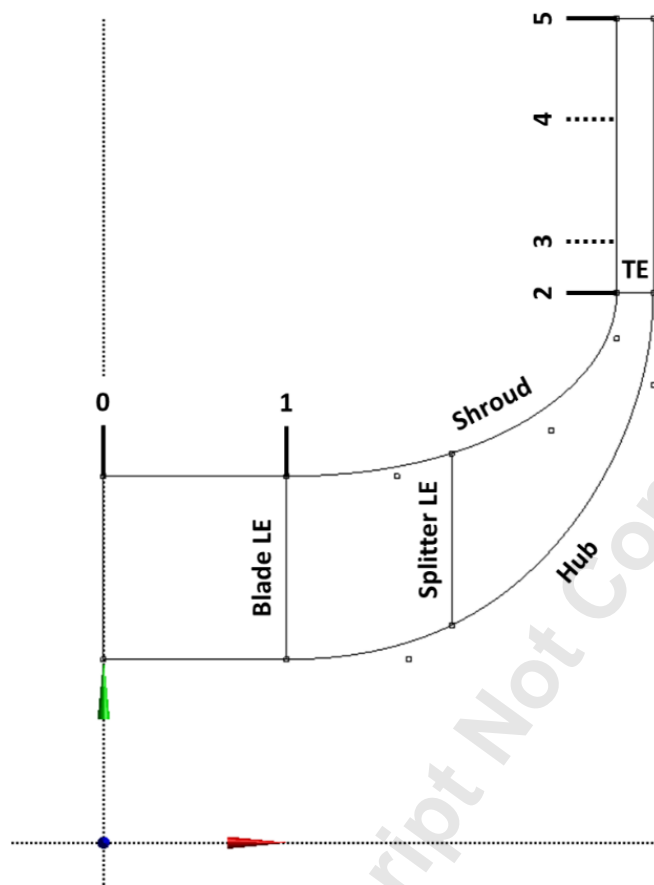
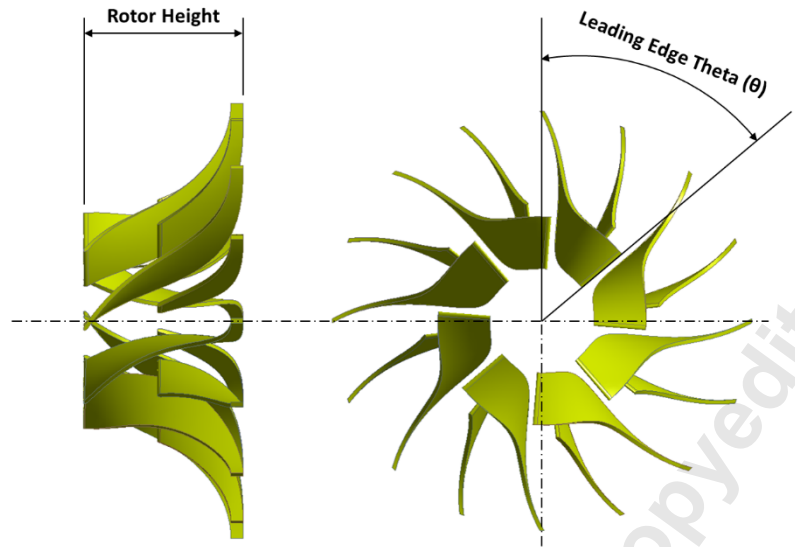


Fig. 4 Parametric meridional view of the centrifugal compressor.

827
828



829

Fig. 5 Optimization parameters of the parameterized rotor geometry.

830

831
832



Fig. 6 Periodic mesh of the centrifugal compressor flow domain.

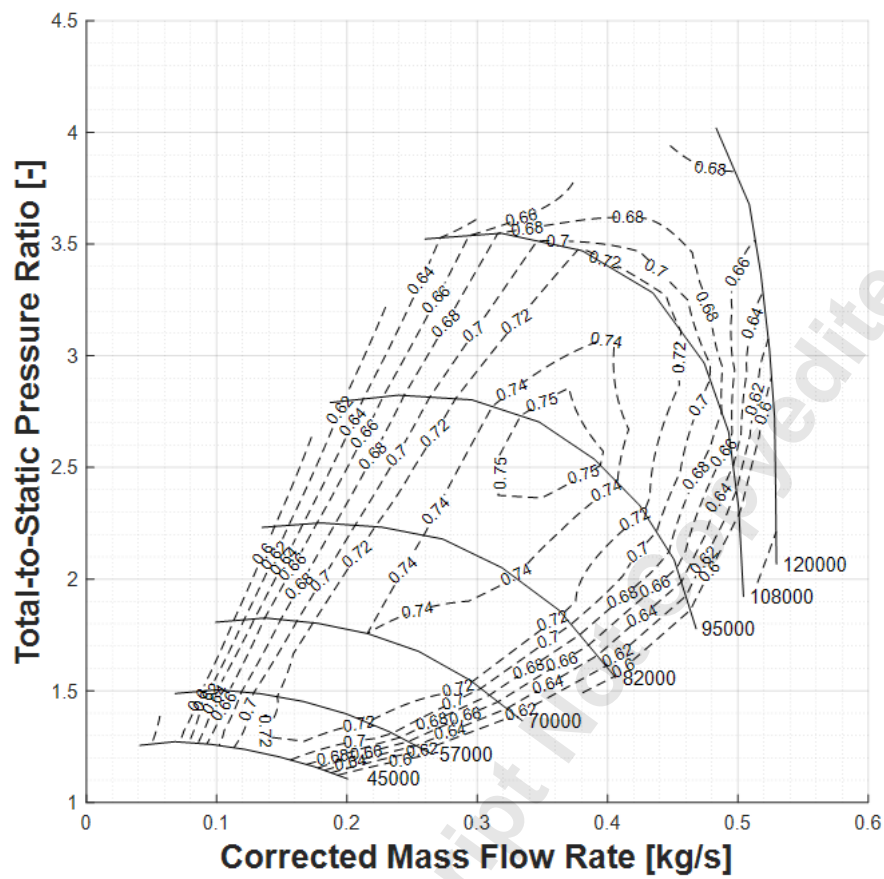
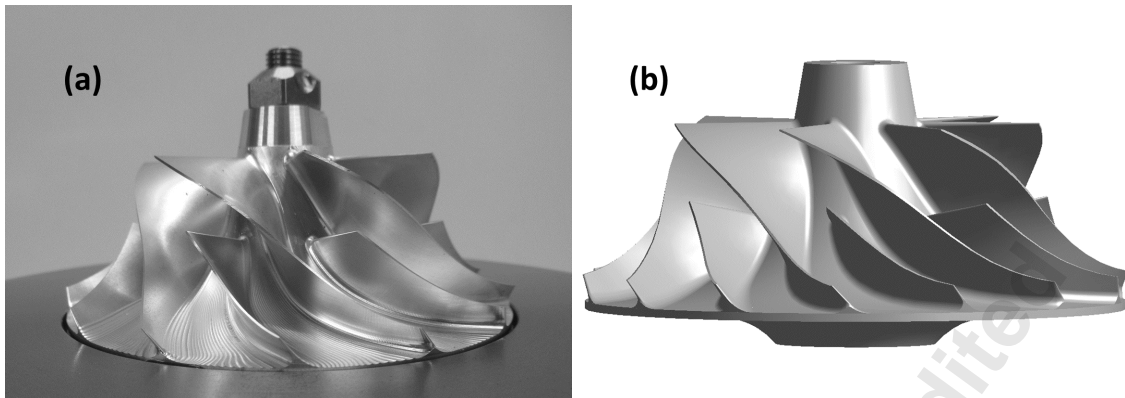


Fig. 7 Compressor performance map of the reference turbocharger.

833

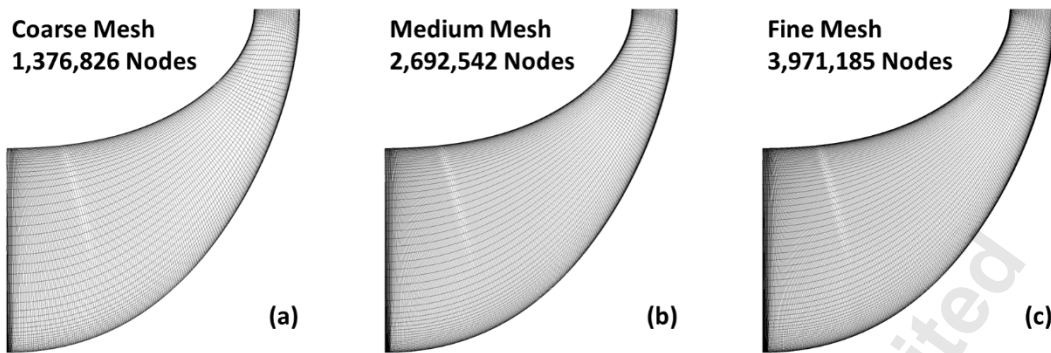
834



835

Fig. 8 (a) The reference compressor and (b) its CAD model.

836



837 **Fig. 9** Three different meshes for the mesh sensitivity: (a) coarse, (b) medium, (c) fine.
838

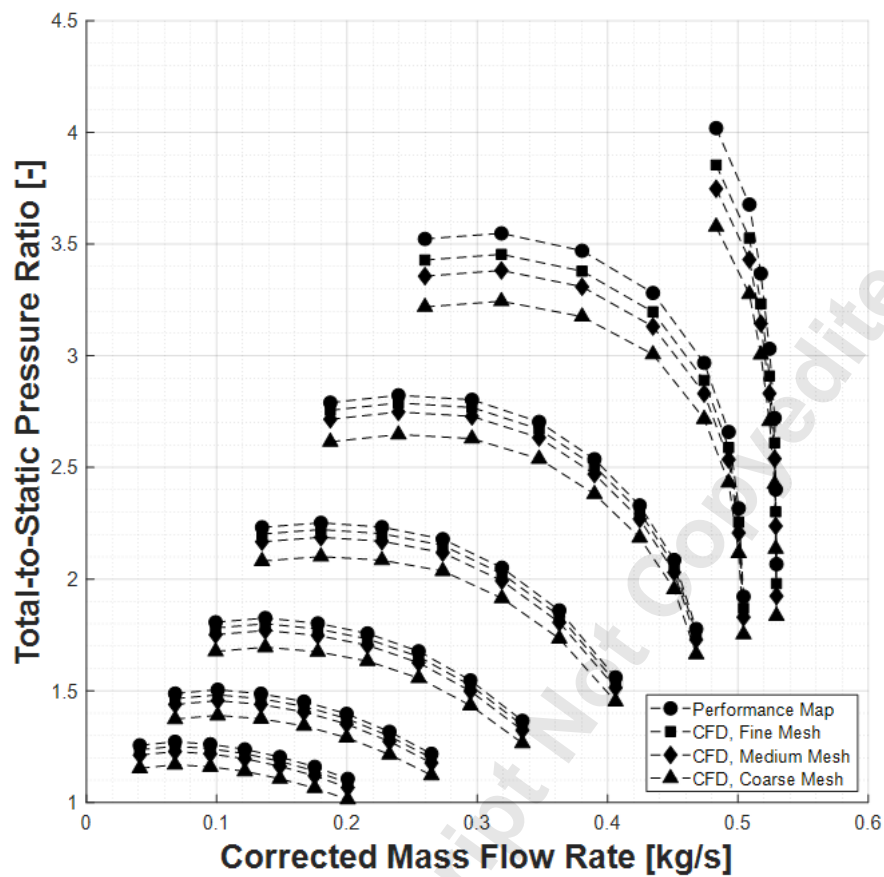


Fig. 10 Comparison of total-to-static pressure ratio CFD results and map data.

839

840

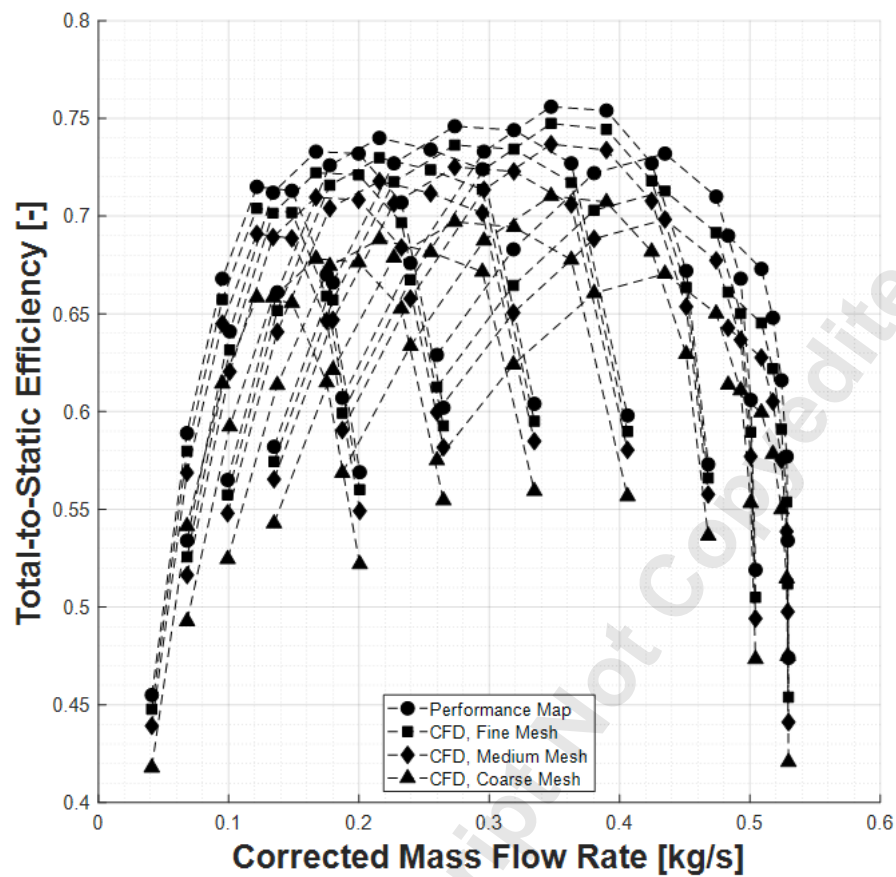


Fig. 11 Comparison of total-to-static efficiency CFD results and map data.

841

842

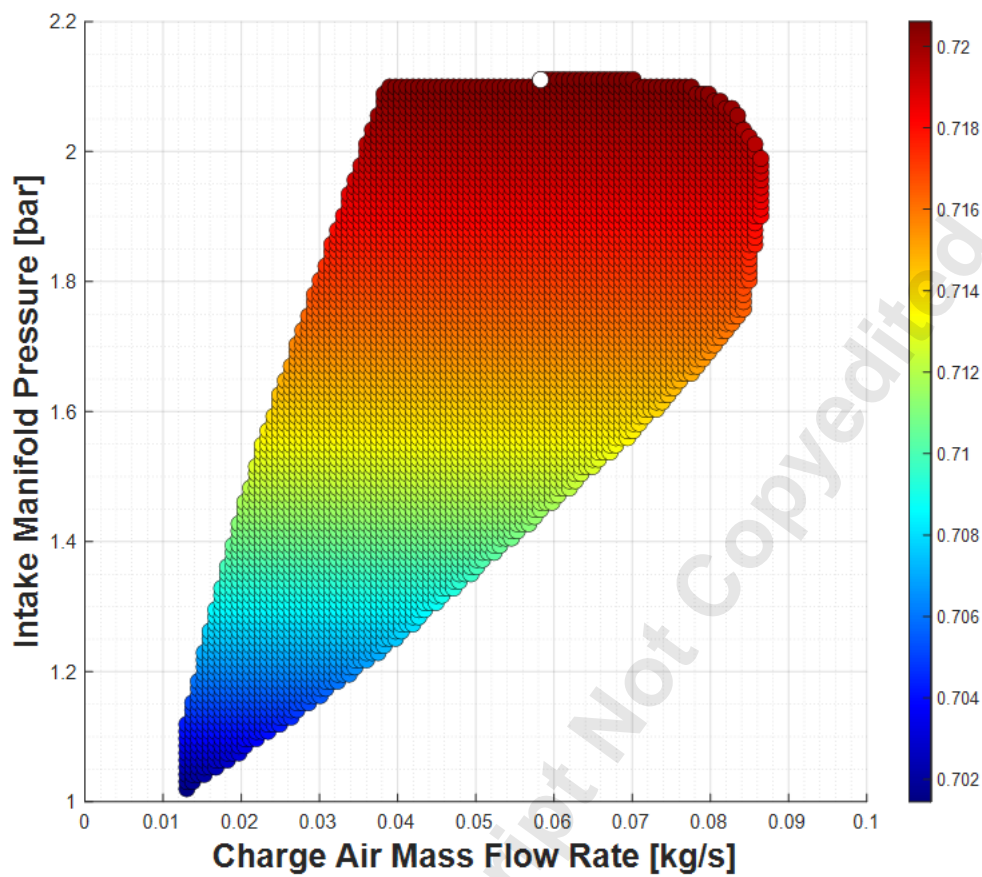


Fig. 12 Efficiency map of the engine operation field.

843

844

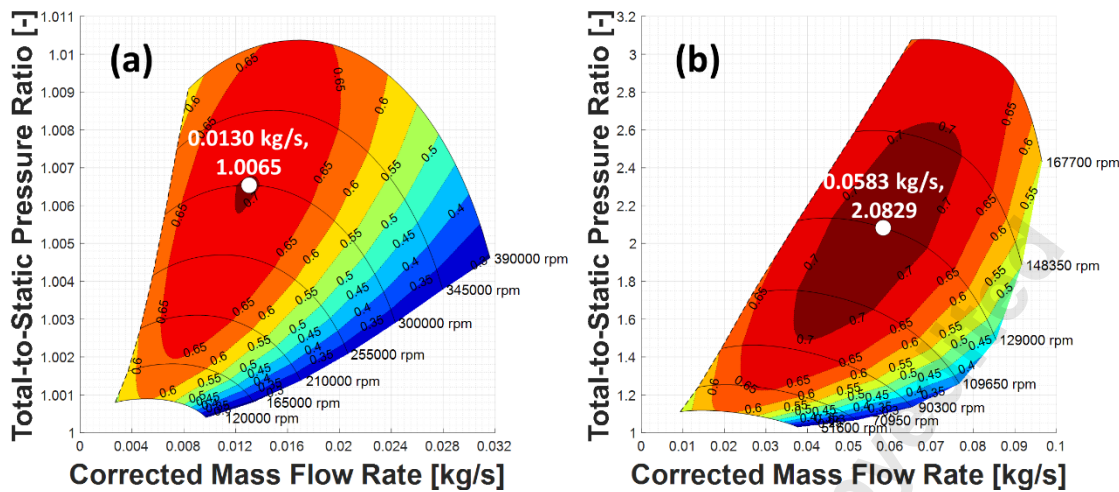
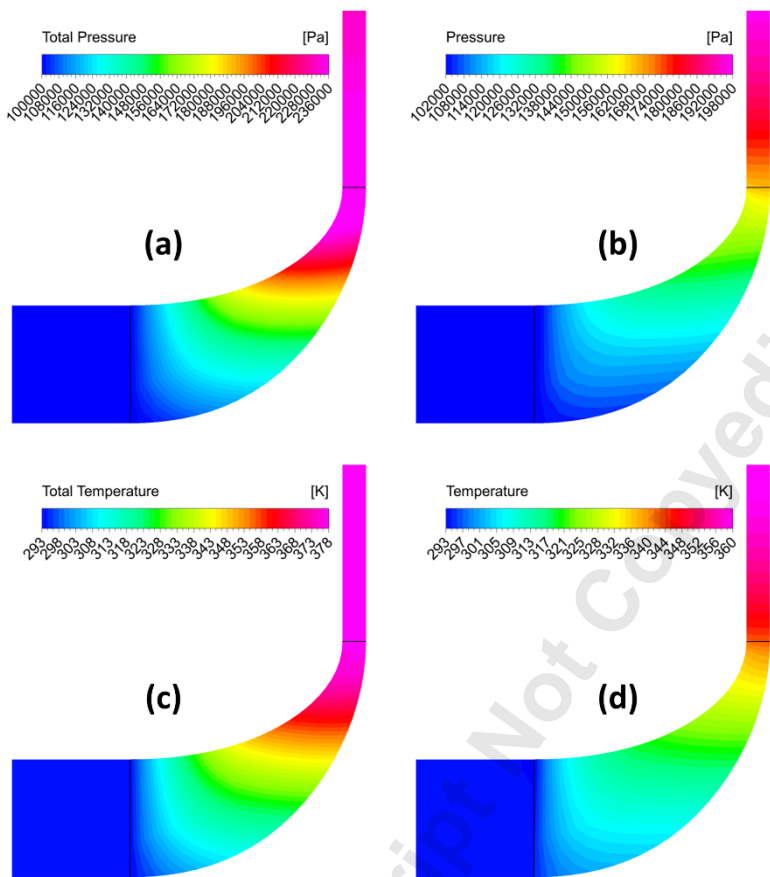


Fig. 13 Comparison of the maps of (a) minimum and (b) maximum design points.

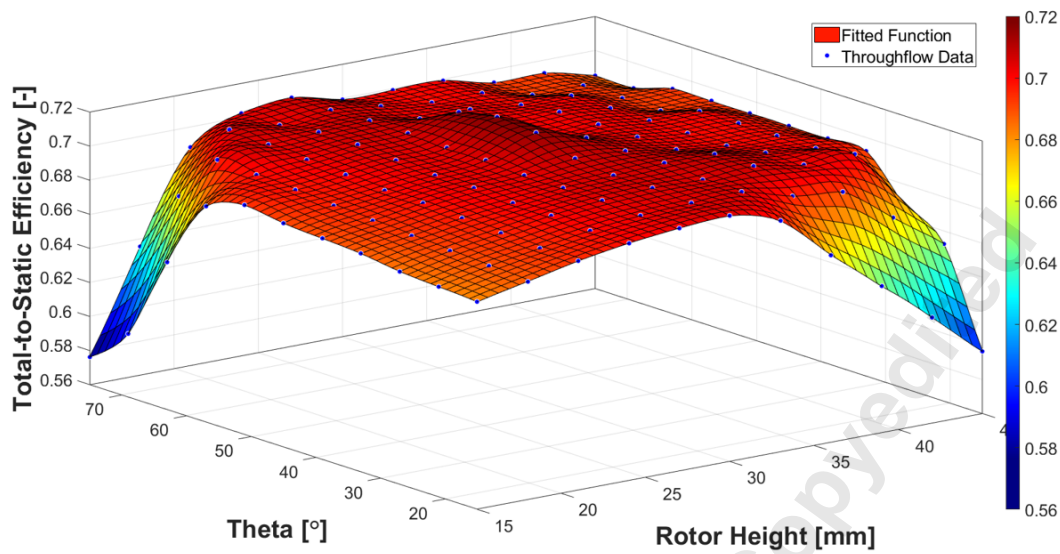
845

846

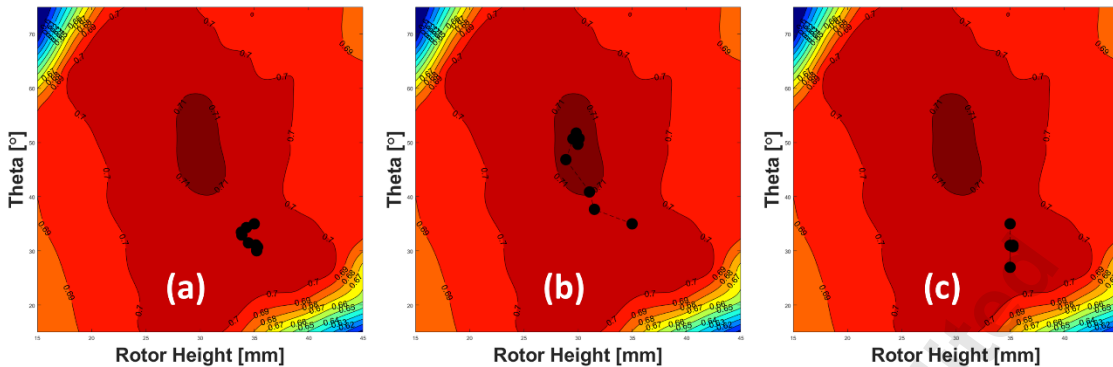


847 **Fig. 14** Throughflow analysis results of the optimum design: (a) p_0 , (b) p , (c) T_0 , (d) T .

848



849 **Fig. 15** Total-to-static efficiency function created from throughflow results.
850



851 **Fig. 16** Converging to different values via (a) NLPQN, (b) NLPDF and (c) PS methods.
852

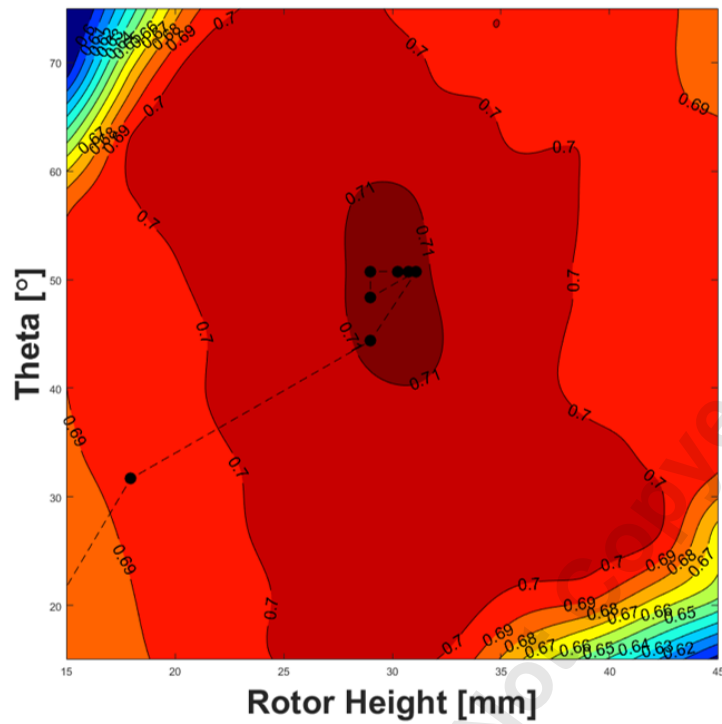
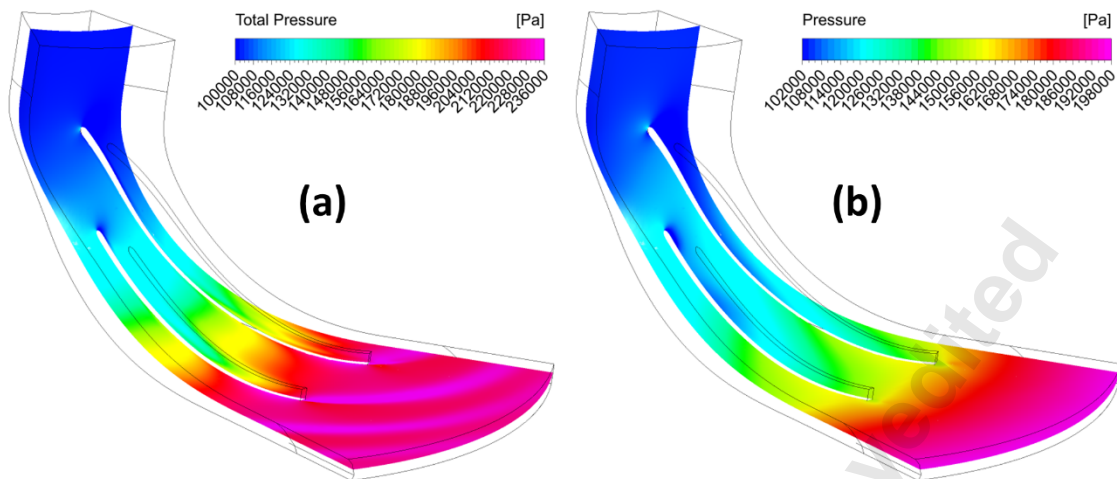


Fig. 17 Genetic algorithm solution.

853

854



855

Fig. 18 3D CFD analysis results of the design point: (a) p_0 , (b) p .